CommSAR: Enabling Bidirectional Communication in SAR Imaging Satellites via Shared Waveform

Yimin Zhao[1], Zhenning Li[2], Hao Pan[1], Hua Li[2], Minhao Cui[4], Jie Xiong[5], Yihai Wei[2,3], Yang Liu[2], Haonan Zhao[2], Mohan Zhang[2,3], Weibo Wang[1], Guihai Chen[1], Kaiyu Liu[2], Linghe Kong[1†]

[1]Shanghai Jiao Tong University [2]Aerospace Information Research Institute, Chinese Academy of Sciences
[3]University of Chinese Academy of Sciences [4]Seoul National University [5]Nanyang Technological University

Abstract

Low Earth Orbit (LEO) Synthetic Aperture Radar (SAR) satellites conventionally rely on dedicated communication links, which impose prohibitive hardware, spectrum, and power overhead as satellite constellations scale. This paper presents *CommSAR*, a novel system that reuses existing SAR imaging waveforms to enable bidirectional communication without modifying satellite hardware or compromising imaging performance. For the downlink, data are embedded by modulating the starting frequency offset of the imaging waveform, preserving the waveform structure and imaging quality. For the uplink, we propose a compact, low-cost programmable metasurface to replace conventional large, expensive antennas, significantly lowering the barrier for dense ground station deployment. To handle extreme satellite dynamics, we employ an opposite-slope waveform as a pilot to compensate for mobility-induced effects. We implement a ground station prototype of *CommSAR* and validate its performance using an in-orbit commercial SAR satellite and a UAV SAR platform. Experimental results show that *CommSAR* preserves imaging performance without degradation while achieving downlink and uplink data rates of up to 105 kbps and 112 kbps, respectively, significantly outperforming the state of the art and demonstrating utility-grade performance.

CCS Concepts

• **Networks** → **Very long-range networks**; *Wireless access networks*; *Network experimentation*; • **Hardware** → *Wireless devices.*

Keywords

LEO satellite, Synthetic Aperture Radar, metasurface

ACM Reference Format:

Yimin Zhao, Zhenning Li, Hao Pan, Hua Li, Minhao Cui, Jie Xiong, Yihai Wei, Yang Liu, Haonan Zhao, Mohan Zhang, Weibo Wang, Guihai Chen, Kaiyu Liu, Linghe Kong. 2026. *CommSAR*: Enabling Bidirectional Communication in SAR Imaging Satellites via Shared Waveform. In *ACM SIGCOMM 2026 Conference (SIGCOMM '26), August 17–21, 2026, Denver, CO, USA.* ACM, New York, NY, USA, 16 pages. https://doi.org/10.1145/3789240.3829144

1 Introduction

With more than 10,000 active satellites currently in operation, space-based networks have become an indispensable global infrastructure [45]. These satellites are broadly classified by their orbital characteristics into three categories: low, medium, and geostationary Earth orbits (LEO, MEO, and GEO). While LEO satellites were traditionally used for Earth observation, recent trends have shifted toward communication services, exemplified by the well-known Starlink constellation [36]. Despite this shift, LEO Synthetic Aperture Radar (SAR) satellites continue to play a critical role in applications such as environmental monitoring and disaster response. To date, more than 200 LEO SAR satellites are operating in space [45].

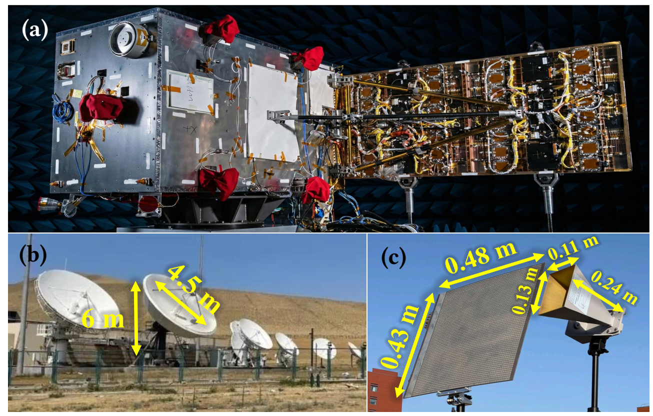

Figure 1: (a) The real-world in-orbit commercial SAR satellite used for experiments. Antennas of (b) a conventional ground station vs. (c) a *CommSAR* ground station.

To achieve high-resolution imaging, these satellites transmit high-power linear frequency-modulated (LFM) pulses through high-performance RF front-ends and offload the acquired imagery via high-speed payload downlinks. Beyond the imaging module, a typical LEO SAR satellite carries another core module: the Telemetry, Tracking, and Command (TT&C) module for satellite control. Although TT&C traffic is far smaller in volume than SAR imagery, it plays a critical role in satellite control by delivering commands for mission tasking, payload control, and anomaly recovery, while returning telemetry that reports the satellite's health and operational status. Unlike payload downlinks, where imagery can be buffered and offloaded later, TT&C traffic is far less delay-tolerant due to its time-critical nature: missing a command opportunity can postpone mission retasking or anomaly recovery until the next available ground contact, typically several hours later.

Because inter-satellite links are not yet widely deployed in current LEO SAR constellations, TT&C functions remain heavily dependent on direct satellite-to-ground communication. Unfortunately, the link between a SAR satellite's TT&C module and a ground station can only be established when the satellite passes over the ground station, which typically lasts only around 10 minutes. Consequently, to improve the responsiveness of ground stations

†Corresponding author: Linghe Kong (linghe.kong@sjtu.edu.cn).

SIGCOMM '26, Denver, CO, USA

ACM ISBN 979-8-4007-2467-1/26/08
https://doi.org/10.1145/3789240.3829144

and increase the total duration a SAR satellite can be connected and controlled, it is essential to increase the number of ground stations deployed. Due to the limited transmit power of the TT&C module, traditional ground stations are typically bulky (see Fig. 1b), relying on high-gain, large-aperture antennas, such as parabolic or Yagi antennas, to capture weak TT&C signals. Moreover, they require costly RF front-end components, including high-performance filters, to achieve effective noise suppression. The substantial hardware and maintenance costs pose a formidable barrier to increasing the deployment density of ground stations.

In this paper, we propose *CommSAR*, an innovative TT&C communication solution for LEO SAR satellites, aimed at reconciling the tension between the demand for timely communication and the prohibitive costs associated with the dense deployment of traditional ground stations. In detail, *we propose leveraging the existing SAR imaging module to serve both sensing and TT&C functions, creating a new side channel for TT&C operations.* Leveraging the high SNR of the SAR imaging signals, we replace conventional large-aperture ground station antennas with a compact combination of a small-sized metasurface and a horn antenna (Fig. 1c). This cost-effective and compact design significantly lowers the barriers to dense ground station deployment. The significantly reduced size also brings the potential to transition from current fixed-location ground stations to mobile ones in the future, enabling far more flexible deployment.

To achieve this, we reuse the LFM waveforms, which are conventionally used exclusively for imaging, to enable bidirectional satellite–ground communication. This shared-waveform design enables each transmitted imaging pulse and its corresponding echo to perform both sensing and communication concurrently. Consequently, the two functions share the same imaging duration, SAR spectrum, and transmit power budget. While prior works have investigated integrated sensing and communication (ISAC) for SAR satellites [49, 53], they all add dedicated communication signals to the LFM waveforms rather than reusing the existing waveforms. This inevitably leads not only to power splitting, which reduces the power allocated to imaging waveforms, but also to interference between the two signals, degrading the imaging performance. More importantly, all of these works support only downlink communication. Existing works supporting uplink communication remain scarce. The state-of-the-art uplink design, SARLink [9], encodes information by modulating the brightness of a small spot in the SAR image using ground-deployed corner reflectors. However, its data rate is below 1 bps, far below even the baseline rates of legacy TT&C systems.

For the downlink in our design, we propose to reuse the existing imaging LFM waveform to embed data, without introducing any additional communication signals. This is nontrivial, as conventional modulation schemes inevitably interfere with the imaging process. In particular, amplitude modulation is fundamentally infeasible because SAR transmitters operate in the deep saturation region at maximum power, while phase and frequency modulation alter the LFM pulse characteristics, resulting in performance degradation of SAR imaging. To address this issue, we propose keeping the waveform shape—essentially a chirp signal in the frequency domain—unchanged, and encoding data solely by varying the starting frequency offset of the waveform. *CommSAR* can thus be deployed on existing SAR satellites via simple waveform parameter configuration, requiring no satellite hardware modifications. Both theoretical analysis and experimental results confirm that this approach introduces a negligible impact on SAR imaging.

For the uplink, if the imaging waveform is not reused for backscatter and an active transmission is instead employed, the transmission must satisfy stringent timing requirements. This is because SAR satellites operate in a pulsed, half-duplex mode, and any transmission outside the narrow pulse window will not be received. We thus adopt a programmable metasurface that modulates the phase of the incident LFM waveform and backscatters it to the satellite, achieving a data rate that is orders of magnitude higher than the state of the art. This approach fully exploits the high peak power of the LFM waveform to enable high-rate backscatter communication. When the metasurface echo arrives at the SAR satellite together with scene echoes, the inherent SAR imaging algorithm serves as a spatial filter, naturally separating the two in the spatial domain. Specifically, it focuses the metasurface echo into one resolution cell while concentrating scene clutter into other cells. In the reconstructed SAR image, each resolution cell spans only one or a few pixels at the native image resolution. This spatial-filtering property guides the uplink modulation choice: frequency modulation can disrupt focusing, while amplitude modulation reduces echo SNR. Consequently, *CommSAR* adopts phase modulation, which preserves SAR focusing without reducing echo SNR. Under this scheme, the metasurface response remains confined to a single resolution cell, leaving the rest of the SAR image unaffected.

Another practical issue we encounter is the high speed of LEO satellites (*e.g.*, ≈7.7 km/s at 344 km altitude), which induces substantial Doppler shifts (up to ±200 kHz) and carrier phase rotations (up to $\pm 8.5 \times 10^7$ deg/s).[1] These dynamics pose significant challenges for demodulating the shared-waveform bidirectional link. In contrast to Starlink, which is designed for communication and uses packetized transmissions with preambles for synchronization and Doppler/phase compensation, the proposed system is built upon pulse-based imaging waveforms. These waveforms contain neither preambles nor pilot symbols, and the short pulse durations leave no room for conventional packet preambles. Moreover, because the satellite–ground station range continuously varies, the received pulses are not uniformly spaced in time. Consequently, timing alignment must be performed on a pulse-by-pulse basis, making mobility compensation significantly more challenging.

To address this mobility issue for the downlink, since the LFM waveform contains the modulated frequency information, it cannot be used to extract the channel Doppler information. *CommSAR* therefore designs and inserts reverse LFM waveforms with the opposite chirp slope as pilots, enabling the estimation and compensation of the Doppler offset. For the uplink, given that satellite displacement is negligible within the 1 μs intra-pulse symbol interval, consecutive symbols experience near-identical phase shifts. *CommSAR* leverages this by employing Differential Binary Phase Shift Keying (D-BPSK), which encodes data in relative phases and inherently cancels mobility-induced phase shift.

This work does not raise any ethical concerns. Our main contributions are summarized as follows:

[1] For a SAR satellite with an altitude of 344 km and a frequency of 9.6 GHz.

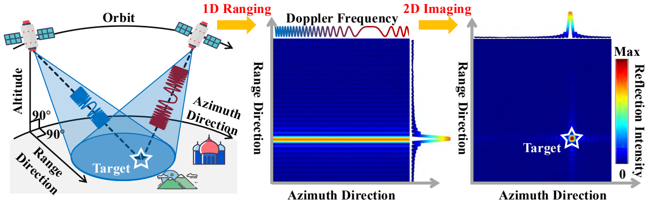

Figure 2: The imaging process for a point target in SAR.

- We propose a novel shared-waveform architecture that enables bidirectional satellite–ground communication by directly modulating SAR imaging pulses and echoes. This approach facilitates seamless integration of sensing and communication without compromising the original imaging performance or requiring any modifications to existing satellite hardware.
- For the uplink, we adopt the latest metasurface technology and fully leverage the high signal power of the imaging SAR waveform to enable backscatter. This approach is much cheaper and more compact than the current antenna design, lowering the barrier for future dense and mobile ground station deployment.
- To mitigate the impairments caused by high LEO satellite dynamics, we adopt delicate signal processing schemes to compensate for mobility-induced Doppler shifts and phase offsets.
- We implement a ground station prototype and conduct extensive real-world experiments using both an in-orbit SAR satellite and a UAV platform. The results demonstrate that *CommSAR* preserves the original imaging performance without degradation, while achieving bidirectional communication rates of up to 105 kbps for the downlink and 112 kbps for the uplink, validating its utility-grade performance and practical feasibility.

2 Background and Preliminary Study

This section introduces the principles of SAR, focusing on two-dimensional image reconstruction through LFM pulse compression in the range and azimuth dimensions. We then characterize the signal profiles of operational SAR satellites using empirical measurements collected from real-world deployments.

2.1 SAR Imaging Primer

We first describe 1D ranging via LFM pulse compression in the range dimension, followed by the formation of the azimuth LFM signal through satellite-induced Doppler modulation, which enables 2D SAR image reconstruction.

1D Ranging with LFM. Similar to conventional radar systems, 1D ranging in spaceborne SAR relies on estimating the time delay of radar echoes. The transmitted LFM pulse is given by

$$s(t) = \mathrm{rect}\left(\frac{t}{T_p}\right) \exp\left(j\pi \frac{B}{T_p} t^2\right), \tag{1}$$

where T_p denotes the pulse duration, B is the bandwidth, and $\mathrm{rect}(\cdot)$ denotes the rectangular window function. For a target at range $R = c\tau_0/2$, where c is the speed of light, the received echo can be expressed as $s(t - \tau_0)$. The target range is then estimated via *pulse compression*, which performs matched filtering by cross-correlating the received echo with a reference replica of the transmitted signal, $s^*(t)$, yielding

$$r(t) = s(t - \tau_0) \otimes s^*(t) \approx T_p \,\mathrm{sinc}\left[B(t - \tau_0)\right]. \tag{2}$$

Pulse compression concentrates LFM energy into a *sinc* waveform, whose mainlobe amplitude scales with pulse duration T_p and its width is inversely proportional to bandwidth B. Leveraging long pulse durations (10–100 μs) and wide bandwidths [2] (up to 1.2 GHz), pulse compression produces a nanosecond-scale correlation peak, enabling sub-meter range resolution.

From 1D Ranging to 2D Imaging. In addition to 1D ranging, SAR requires additional azimuth (along-track) information to achieve 2D imaging as illustrated in Fig. 2. Prior to azimuth compression, range cell migration correction (RCMC) is performed to realign target trajectories that have migrated across range bins due to the satellite's motion. As the satellite travels at velocity v, it repeatedly illuminates the same ground target and receives echoes over multiple pulses over time. Let η denote the slow-time (azimuth-time) index corresponding to successive pulse transmissions along the satellite flight direction. The pulse with $\eta = 0$ corresponds to the first illumination of the target, while $\eta = \eta_0$ represents the closest-approach instant, at which the slant range attains its minimum value R_0. Accordingly, the slant range as a function of the pulse index η can be expressed as

$$R(\eta) = \sqrt{R_0^2 + v^2(\eta - \eta_0)^2} \approx R_0 + \frac{v^2(\eta - \eta_0)^2}{2R_0}. \tag{3}$$

The target's azimuth position can then be determined by identifying the pulse index $\eta = \eta_0$. For high-resolution estimation, the Doppler shift induced by the satellite's motion along the azimuth direction is exploited, as the slant range between the satellite and the target varies with η as

$$f_D(\eta) = -\frac{2}{\lambda}\frac{dR(\eta)}{d\eta} \approx -\frac{2v^2}{\lambda R_0}\eta, \tag{4}$$

where λ is the radar wavelength. Notably, this Doppler frequency varies approximately linearly with η, producing an LFM structure in the azimuth dimension. Consequently, an azimuth matched filter, analogous to the range pulse compression filter, coherently compresses the target energy into a single two-dimensional resolution cell, producing *2D imaging*.

It should be noted that the aforementioned 2D pulse compression serves as the foundational front-end shared by the vast majority of practical SAR imaging algorithms. Subsequent back-end procedures, such as Range-Doppler [2], Omega-K (ω-K) [4], Chirp Scaling [31], Back Projection [43], and Polar Format Algorithm [48], operate exclusively on the focused signals produced at this stage. Consequently, any modulation that distorts the pulse-compression response propagates residual errors throughout the entire imaging chain. To avoid the cost and risk of modifying this well-established processing pipeline, existing SAR-ISAC downlink approaches [49, 53] typically superimpose auxiliary communication signals while preserving the integrity of the original radar waveform.

2.2 In-orbit SAR Satellite Characteristics

Based on our in-orbit LEO SAR satellite platform (Fig. 1a), we conduct two sets of measurements. First, we show the relationship between TT&C availability and global ground station (GS) placement, motivating the design of *CommSAR*. Second, we measure the

[2] Typical SAR bandwidths include 100 MHz for C-band, 600 MHz for X-band, and 1200 MHz for Ka-band.

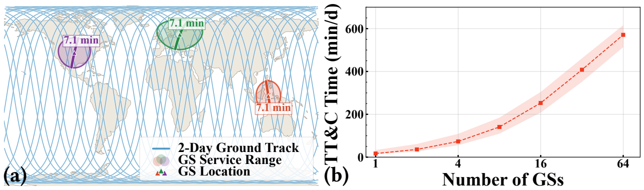

Figure 3: Based on the orbit of our in-orbit SAR satellite, (a) shows its two-day ground track and representative GS service ranges at different latitudes, with highlighted arcs denoting typical per-pass TT&C contact windows; (b) shows the aggregate daily TT&C contact time versus the number of globally deployed GSs under random land placement.

bidirectional RF signals exchanged between the satellite and the GS over satellite passes, demonstrating the feasibility of *CommSAR*'s shared-waveform design under operational channel conditions.

TT&C-GS Relationship. Typical LEO satellites operate in high-inclination orbits, allowing their ground tracks to sweep across the Earth as it rotates and provide global coverage. For our in-orbit satellite, Fig. 3a shows its ground track over a two-day period in October 2025. We overlay three representative real-world GSs at different latitudes. Each GS can establish TT&C contact with the satellite only when the satellite enters the GS's antenna coverage, which is typically defined by a minimum elevation angle of 5°. The corresponding service regions are illustrated as circular coverage areas in Fig. 3a. Although the satellite completes multiple orbits around Earth during the 48-hour observation period, the three GSs collectively provide only about 20 TT&C opportunities, with the longest contact lasting just 7.1 minutes. Consequently, under this sparse GS deployment, the satellite is commandable for only approximately 20×7.1 minutes, corresponding to just 4.9% of the two-day period. To improve control-plane connectivity, operators must deploy a large number of GSs worldwide. Fig. 3b quantifies this relationship, showing that the aggregate TT&C contact time increases with GS deployment density. However, conventional GSs are costly, physically large, and require country-specific spectrum licenses for active uplink transmission, making dense global deployment prohibitively expensive. This motivates *CommSAR*: by leveraging the SAR satellite's high-power radar waveform, *CommSAR* eliminates the need for active uplink transmission, significantly reduces GS hardware complexity, simplifies worldwide deployment, and ultimately expands the available TT&C contact window.

SAR Signal Characteristics. Using the *CommSAR* GS prototype (Fig. 11c), we capture downlink radar pulses transmitted by our in-orbit SAR satellite. In collaboration with the satellite operator, we also obtain onboard IQ recordings of the corresponding ground-reflected echoes. Together, these paired measurements characterize both propagation paths: the downlink signal received at the GS and the uplink echo reflected from the ground back to the satellite.

The RF specifications of the investigated SAR satellite are detailed in Fig. 4a. This satellite transmits LFM pulses centered at 9.6 GHz with a bandwidth of 600 MHz and a transmit power of *68.06 dBm (≈6.4 kW)*. For our measurements, the pulse duration (T_p) and duty cycle are configured to 15 μs and 10%, respectively, yielding a 150 μs pulse repetition interval. Fig. 4b illustrates the spectrogram of the ground-received signal. As ground-reflected replicas, the satellite-captured echoes preserve the same time-frequency structure, differing only in propagation delay, Doppler shift, and attenuation.

Antenna Type	2D Scanning Planar Active Phased Array	**Center Frequency**	9.6 GHz
Bandwidth (B)	600 MHz	**Polarization**	HH
Antenna Aperture	3.8 m (az) × 0.73 m (rg)	**T/R Channels**	10 (az) × 32 (rg)
Pulse Duration (T_p)	10-100 μs	**PRF Range**	2-8 kHz
Beamwidth	0.42° (az) × 2.17° (rg)	**Scan Capability**	± 1°
Average Transmit Power during LFM Pulse	68.06 dBm (**6,400 W**)	**Average Transmit Power**	≤ 61.07 dBm (1,280 W)

(a) RF specifications of our in-orbit SAR satellite.

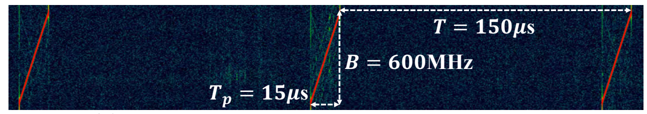

(b) Spectrogram of ground-received SAR signals.

Figure 4: Real-world measurements of our in-orbit SAR satellite.

Next, we characterize the signal strength of SAR transmissions at the ground receiver and the intensity of echoes reflected back to the satellite. Typically, SAR satellites perform imaging only during an overpass when the elevation angle exceeds 30°.[3] Across multiple overpasses within this 30° to 90° range, the measured ground SNR consistently falls between 18 and 27 dB. This high SNR is sustained by the satellite's *spotlight mode*, which actively steers the antenna beam to illuminate the target area.[4] Although echo SNR inherently varies with terrain reflectivity, strong point reflectors, such as a reflective metal plane or our custom metasurface (Fig. 1c), achieve significant SNR after spatial filtering (Sec. 3.2). Empirical measurements show that, during a 30°-elevation-angle overpass, our metasurface achieves an echo SNR of up to 10 dB at the satellite receiver. Similarly high SNRs are maintained across a broad range of overpass elevation angles, ensuring reliable link quality. Together, these measurements demonstrate that both native SAR transmissions and metasurface echoes provide sufficient power budgets for shared-waveform communication.

3 System Design

We propose *CommSAR*, a shared-waveform design that enables bidirectional satellite–ground communication by leveraging the native imaging waveforms of spaceborne SAR satellites. An overview of the *CommSAR* framework is presented in Fig. 5, which also details the bidirectional waveforms and resulting imaging quality in comparison with standard SAR. *CommSAR*'s primary objective is to embed bidirectional data into native SAR pulses and echoes without compromising SAR imaging performance. To this end, this section details three core design components tailored to address the specific challenges of downlink transmission, uplink reflection, and extreme LEO satellite mobility.

3.1 Shared Waveform for Downlink

Information embedding in LFM signals can be categorized into two schemes. The intra-pulse scheme embeds data within a single pulse

[3]The elevation angle is defined as the angle between the satellite-to-target line of sight and the local tangent plane.

[4]Spotlight mode includes sliding spotlight and staring spotlight modes. These established high-resolution SAR modes are increasingly supported by agile commercial SAR systems [5, 13, 14, 44, 50]. We discuss the scope of these imaging modes in Sec. 6.

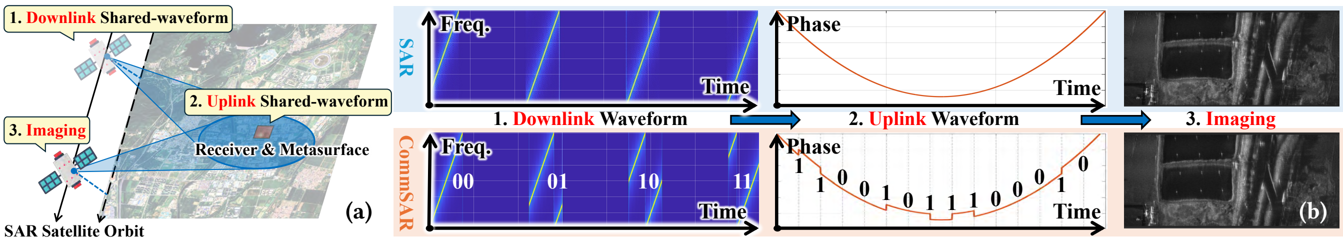

Figure 5: Overview of *CommSAR*: (a) the system pipeline; (b) comparison between standard SAR and *CommSAR*.

by modulating amplitude, phase, chirp slope, or chirp starting frequency. The inter-pulse scheme, by contrast, operates across pulses, *e.g.*, pulse repetition interval (PRI) modulation. However, the stringent requirement to preserve imaging fidelity precludes most of these options. Specifically, in SAR satellite systems, high-power amplifiers (HPAs) operate in a deep saturation region and necessitate a constant envelope, rendering amplitude modulation (AM) infeasible. Phase modulation (PM) disrupts azimuth coherent processing, introducing phase errors that lead to azimuth defocusing and image artifacts. Furthermore, chirp slope modulation disrupts echo energy uniformity, while PRI modulation jeopardizes the precise timing of onboard data acquisition and IQ storage. Consequently, we draw inspiration from the *LoRa* protocol [37] in the IoT domain and adapt its core modulation concept—*cyclic-shift chirp keying*—to the SAR context. The resulting waveform is referred to as *cyclic-shifted LFM (CS-LFM)*, with each pulse representing one symbol. We next detail the CS-LFM-based downlink communication and show why it is the only viable non-destructive scheme that preserves imaging fidelity.

CS-LFM Modulation. Suppose a standard LFM pulse sweeping a bandwidth B and spanning a pulse duration of T_p is denoted as $s(t)$, where $0 \le t \le T_p$. *CommSAR* modifies the standard LFM pulse by applying a cyclic time shift. Specifically, an input symbol index $n \in \{0, 1, \ldots, N_{\text{sym}} - 1\}$ is mapped to a discrete cyclic shift of time $\Delta t_n = \frac{n}{N_{\text{sym}}} T_p$. The n-th CS-LFM waveform is then expressed as

$$s_{\text{cs}}^{(n)}(t) = s\big((t + \Delta t_n) \bmod T_p\big)\,. \tag{5}$$

For example, the CS-LFM illustrated in Fig. 6a is formed by cyclically shifting the standard LFM in Fig. 6b by Δt_n=11.25μs with T_p=15μs, N_{sym}=256 and n=192.

Preamble-Free Downlink Time Synchronization. *CommSAR* performs pulse-wise detection and time synchronization directly in the magnitude domain by leveraging the inherently high SNR of SAR downlink signals. However, because the received signal strength varies with satellite pass geometry, static magnitude thresholds cannot provide robust pulse detection. To address this, we propose a "coarse-to-fine" adaptive synchronization strategy.

(1) Coarse Detection (Energy-based Triggering): Suppose a buffer of received IQ samples is denoted as $\{r[i]\}_{i=0}^{N-1}$, where i is the sample index and N is the buffer length. First, a robust estimate of the background noise floor is obtained by smoothing the received samples with a sliding window of length L. To suppress impulsive interference without excessively smoothing the pulse onset, L is empirically set to 1% of the pulse duration. This smoothing process yields the data representation: $y[i] = \frac{1}{L}\sum_{k=0}^{L-1}|r[i-k]|, i \in [L-1, N-1]$. The background noise magnitude level is then estimated as the p-quantile:

$$\hat{E}_{\text{bg}} = y_{\text{sorted}}[\lfloor p \cdot (N-1) \rfloor]\,, \tag{6}$$

where $\{y_{\text{sorted}}[i]\}_{i=0}^{N-1}$ is $\{y[i]\}_{i=0}^{N-1}$ sorted in ascending order. The detection threshold is defined as $\alpha \hat{E}_{\text{bg}}$, where α is a sensitivity scaling factor. To ensure robust performance, we set $\alpha = 2.5$ using median estimation ($p = 0.5$). The first index at which the smoothed magnitude exceeds this adaptive threshold is recorded as the coarse trigger, indicating the presence of a pulse

$$i_{\text{trig}} = \min\left\{ i \mid y[i] > \alpha \hat{E}_{\text{bg}} \right\}. \tag{7}$$

(2) Fine Synchronization (Half-power Backtracking): After detection, to recover the precise start time, a local search is performed preceding i_{trig}. Let $i_{\text{peak}} = \arg\max_{i \in [i_{\text{trig}}-2L,\, i_{\text{trig}}]} |r[i]|$ and $V_{\text{peak}} = |r[i_{\text{peak}}]|$. The estimated pulse start (*i.e.*, the magnitude rising edge), denoted as $\hat{i}$, is obtained by backtracking to the half-power point:

$$\hat{i} = \max\left\{ i < i_{\text{peak}} \;\middle|\; |r[i]| < V_{\text{peak}}/\sqrt{2} \right\} + 1. \tag{8}$$

In this way, we can achieve preamble-free timing synchronization for each downlink pulse.

Demodulation. Following pulse-wise synchronization, CS-LFM demodulation is implemented via dechirping, *i.e.*, multiplying the received signal by a conjugated standard LFM reference. As depicted in Fig. 6c, this process transforms the CS-LFM waveform into a dual-tone signal in the frequency domain, with peak frequencies at $f_1 = f_{\text{sym}} + B/2$ and $f_2 = f_{\text{sym}} - B/2$. Consequently, by maintaining a sampling rate $f_s \ge 2B$ to mitigate aliasing, we can identify these two spectral peaks via an FFT operation, enabling symbol detection.

Downlink Data Rate Analysis. The achievable data rate is fundamentally limited by the orthogonality among communication symbols. Specifically, over a pulse duration T_p, the minimum resolvable frequency spacing is $\Delta f = 1/T_p$, which yields at most $B/\Delta f = BT_p$ mutually orthogonal symbols per pulse. With a pulse repetition frequency (PRF) of f_{PRF}, the maximum achievable downlink data rate is

$$R_{\text{down}} = f_{\text{PRF}} \log_2(BT_p). \tag{9}$$

For our in-orbit testbed (B=600 MHz, T_p=15 μs, f_{PRF}=8 kHz at the maximum PRF), this yields $R_{\text{down}} \approx$105 kbps, which is sufficient to support typical satellite TT&C requirements.

High-Fidelity SAR Imaging. Preserving native SAR imaging performance is a critical requirement for the proposed downlink. As discussed in Sec. 2.1, all SAR imaging algorithms rely on the initial two-dimensional pulse compression. Therefore, if this stage produces the same response as a standard LFM waveform, all subsequent imaging processing remains unaffected. CS-LFM directly

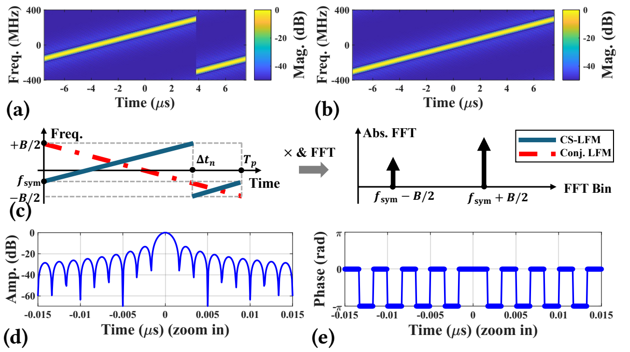

Figure 6: (a, b) Spectrogram of a CS-LFM symbol and a standard LFM waveform. (c) Demodulation process of a CS-LFM symbol. (d, e) After pulse compression, both LFM and CS-LFM produce identical amplitude and phase responses.

exploits this property by applying a cyclic time shift to the standard LFM pulse, which preserves the signal envelope and spectral magnitude while introducing only a deterministic phase rotation in the frequency domain. Consequently, pulse compression, performed by cross-correlating the received pulse with a symbol-specific replica, produces a sinc mainlobe response identical to that of standard LFM (Fig. 6). As a result, both the range-compressed response and the subsequent azimuth compression remain consistent with those of conventional SAR, thereby preserving overall imaging fidelity.

The equivalence between CS-LFM and conventional LFM pulse compression strictly holds when the processing window is limited to the pulse duration. In practice, however, SAR receivers capture additional noise-filled samples beyond the pulse boundaries, making the two waveforms no longer mathematically identical. Nevertheless, the differences are minor edge effects and have a negligible impact on SAR imaging performance, as validated in Sec. 5.3.

3.2 Shared Waveform for Uplink

By leveraging the satellite's high-power CS-LFM pulses as the uplink carrier, *CommSAR* embeds data into reflected echoes via a programmable metasurface. This architecture exploits the native SAR imaging pipeline as a high-gain spatial filter, enabling the extraction of modulated signals from background clutter. For modulation, we adopt an intra-pulse scheme to achieve a higher data rate than inter-pulse modulation. This choice is also motivated by the characteristics of the space–ground channel and the underlying SAR imaging physics. Specifically, amplitude modulation reduces the effective echo SNR, while frequency modulation perturbs the echo spectrum, leading to spatial defocusing or target displacement in the reconstructed image. In contrast, phase modulation preserves the integrity of the 2D pulse compression process, making it transparent to SAR imaging. We next present the programmable metasurface-based uplink communication framework.

Intra-Pulse Phase Modulation and Demodulation. As shown in Fig. 6e, the CS-LFM waveform inherently preserves the underlying quadratic phase structure. We implement binary phase modulation by superimposing discrete phase offsets $\phi_k \in \{0, \pi\}$ onto this echo pulse via a programmable metasurface. At the SAR satellite's receiver, demodulation is performed via dechirping, which involves multiplying the received signal by the complex conjugate of a replica of the downlink CS-LFM waveform. This operation coherently cancels the quadratic phase history of the carrier, thereby isolating the embedded binary information in the residual phase of the dechirped signal. Notably, although CS-LFM introduces a transient phase ramp at the cyclic shift instant, our SAR satellite signal measurements (Fig. 11a) show that this effect is confined to the nanosecond timescale. Since this duration is several orders of magnitude shorter than the μs-scale phase-modulated symbols, its impact on data demodulation is negligible.

Programmable Metasurface. We develop a reflective programmable metasurface capable of high-speed phase modulation. As illustrated in Fig. 7, the metasurface comprises periodically arranged meta-atoms. To implement these binary phase states, the meta-atoms are specifically engineered to provide two distinct reflective phase states with a phase difference near 180°, maximizing their distinguishability. This dual-state modulation is realized by toggling the states of diodes integrated into the top layer of each meta-atom. The proposed metasurface is highly scalable. By tuning the structural parameters of its metallic patterns, it can be adapted to support a wide range of SAR operating frequencies. Detailed design specifications for different frequency bands are provided in Fig. 7. Operationally, a single controller synchronously drives the diodes across all meta-atoms, allowing the entire surface to switch phase states uniformly. This architecture can achieve a stable switching rate of up to 1 MHz in our prototype implementation.

Furthermore, the meta-atom is designed to maintain a stable phase difference between its two states over a wide frequency band, ensuring stable modulation despite rapid CS-LFM frequency variation. This wideband design offers a practical advantage: by scaling the meta-atom dimensions [28], the metasurface can be optimized to support nearly all global SAR satellites operating across the L-, C-, X-, Ku-, and Ka-bands using only five optimized designs. Fig. 7 illustrates the structural design and the five scaled geometries, with detailed dimensions provided in Appendix A. Fig. 8a further presents the measured phase difference ($\Delta\Phi$) between the two modulation states for each size, demonstrating stable near 180° phase separation across the corresponding operating band. Fig. 8b further presents the numerical results showing that the radar cross-section (RCS) difference between the designed metasurface and a perfect electric conductor (PEC) is negligible.

Uplink Data Rate Analysis. The achievable uplink data rate is jointly determined by the pulse duration T_p, the binary phase modulation frequency f_{PSK}, the pulse-detection timing reservation, and the pulse repetition frequency f_{PRF}:

$$R_{\text{up}} = f_{\text{PRF}} \left(f_{\text{PSK}} T_p - 1 \right). \quad (10)$$

For our in-orbit testbed ($f_{\text{PRF}} = 8$ kHz at the maximum PRF, $T_p = 15\ \mu$s) and metasurface implementation ($f_{\text{PSK}} = 1$ MHz), this yields an uplink data rate of $R_{\text{up}} = 112$ kbps. One symbol is reserved for pulse detection and trigger synchronization, as described below.

Uplink Time Synchronization. To ensure precise temporal alignment, the metasurface controller is coupled with the downlink receiver (Fig. 11c). In practice, this timing is met locally at the GS: the downlink receiver continuously monitors the incident pulse energy, and the pulse detector in Eq. (7) produces a hardware trigger as soon as the pulse onset is detected. This trigger is directly wired

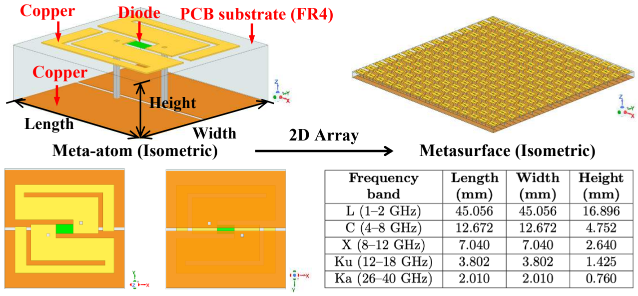

Frequency band	Length (mm)	Width (mm)	Height (mm)
L (1–2 GHz)	45.056	45.056	16.896
C (4–8 GHz)	12.672	12.672	4.752
X (8–12 GHz)	7.040	7.040	2.640
Ku (12–18 GHz)	3.802	3.802	1.425
Ka (26–40 GHz)	2.010	2.010	0.760

Figure 7: The programmable meta-atom and its metasurface.

to the metasurface controller, avoiding software scheduling or network delay. The controller then modulates a sequence comprising a *Barker preamble* [3] followed by data symbols. The Barker code is chosen for its favorable autocorrelation properties, enabling rapid and precise synchronization at the satellite receiver through cross-correlation. For our 15 μs pulse and 1 MHz metasurface switching rate, the controller reserves approximately one symbol interval for pulse detection and trigger propagation, and then emits a 14-symbol modulation sequence over the remaining pulse duration.

Spatial Filtering-Based Metasurface Echo Extraction. The primary challenge in the uplink is the intense background clutter, arising from the superposition of echoes from millions of ground scatterers, which interferes with the modulated reflections from the metasurface. The key observation for addressing this challenge is that standard SAR focusing inherently acts as a high-gain spatial filter, naturally suppressing this interference. After focusing, echoes from different ground patches are mapped to their corresponding range–azimuth resolution cells: the metasurface response is concentrated in the known GS cell, while the background clutter is focused into other cells. Because the GS location is known, *CommSAR* does not require a blind search over the scene. Instead, it directly reuses the standard focused SAR image and extracts the range–azimuth resolution cell corresponding to the metasurface for communication recovery. The extracted resolution cell is an image-domain representation, whereas D-BPSK decoding requires a time-domain echo. *CommSAR* therefore employs a post-focusing recovery branch to reconstruct the time-domain echo:

(1) *Focus Search:* The satellite performs standard 2D SAR focusing on a short echo buffer (*e.g.*, 0.5 s) and crops the known GS cell. As a result, the computational cost is dominated by standard SAR focusing rather than by the location lookup.
(2) *Echo Rebuild: CommSAR* applies inverse focusing to the selected cell to reconstruct a clutter-suppressed time-domain echo.
(3) *D-BPSK Decoding:* The reconstructed echo is dechirped and demodulated to recover the uplink symbols from the residual phase, following the D-BPSK scheme described in Sec. 3.3.

The focusing buffer duration controls the selectivity of this spatial filter. A longer buffer extends the synthetic aperture and improves azimuth resolution, reducing the ground area covered by the selected resolution cell and thereby admitting less surrounding clutter. However, it also increases the number of pulses processed during SAR focusing and inverse focusing, resulting in higher computational cost and longer processing latency. Consequently, uplink demodulation exposes a tunable latency–selectivity trade-off.

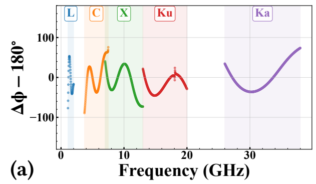

(b)

	PIN-On	PIN-Off	PEC
L (@1.5 GHz)	-15.67	-15.87	-15.04
C (@6 GHz)	-17.72	-17.7	-17.4
X (@9.5 GHz)	-17.9	-18	-17.65
Ku (@16 GHz)	-17.78	-17.8	-17.75
Ka (@35 GHz)	-17.93	-17.96	-17.88

Figure 8: (a) Measured phase difference ($\Delta\Phi$) between the two modulation states for five meta-atom sizes. (b) Total RCS (dBsm) comparison under different configurations.

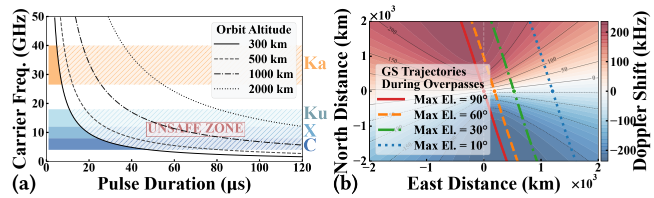

Figure 9: (a) Reliability of conventional Doppler compensation based on TLE/SGP4. (b) GS trajectories within the satellite's footprint during overpass events with different maximum elevation angles (Max El.).

3.3 Managing Extreme LEO Mobility

The extreme velocity of LEO SAR satellites ($\approx$ 7.7 km/s) poses critical challenges. In the downlink, Doppler shifts distort the dechirped frequency, hindering symbol decoding. In the uplink, rapid path-length variations introduce severe phase uncertainty for phase-modulated signals. In this section, we detail the strategies used to mitigate these mobility-induced effects.

Opposite-Slope LFM as Doppler Pilots. A natural alternative is for the ground receiver to precompute the expected Doppler shift using orbital information, such as public Two-Line Element (TLE) data [15] propagated with the SGP4 model [46]. However, such predictions are inherently coarse. Because TLEs represent mean orbital elements rather than instantaneous state vectors, they can introduce position errors of tens of kilometers, resulting in significant residual Doppler errors [30, 33]. Residual Doppler impact is governed by carrier frequency, orbital altitude, and pulse duration (T_p). At high frequencies, long pulses, or low altitudes, this residual can exceed the symbol tolerance $\Delta f/2 = 1/(2T_p)$, compromising demodulation reliability. This defines an "Unsafe Zone", as illustrated in Fig. 9a, where for a fixed altitude, combinations of higher carrier frequency and longer T_p (above and to the right of the curve) incur residual Doppler exceeding the symbol decoding tolerance.

To overcome this limitation, *CommSAR* draws inspiration from pilot symbols in conventional communication systems and occasionally inserts opposite-slope LFM pilot pulses in place of data symbols. The opposite slope serves a dual purpose. First, it ensures reliable discrimination from regular data symbols. Because all CS-LFM data symbols share the same chirp slope, the opposite-slope pilot can be readily identified at the receiver through correlation. Second, reversing the slope preserves the waveform's time–bandwidth product and power spectral density, leaving the pulse compression response unchanged. This makes the pilots fully transparent to the legacy SAR imaging pipeline, introducing no observable degradation in imaging performance.

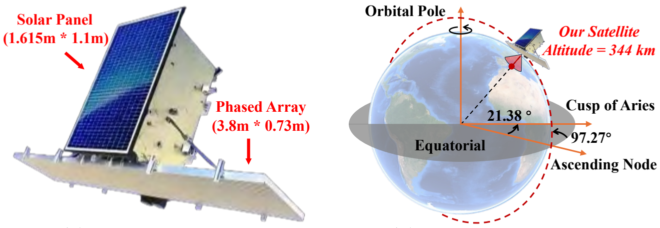

(a) System model. **(b) Orbital trajectory.**

Figure 10: In-orbit SAR satellite testbed.

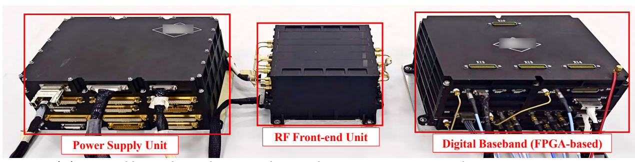

(a) Satellite-hardware-based *CommSAR* radar prototype.

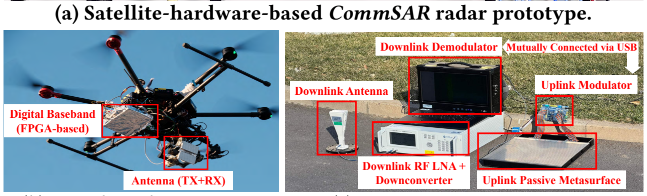

(b) UAV-based *CommSAR* radar prototype. **(c) *CommSAR* GS prototype.**

Figure 11: *CommSAR* system prototypes.

The detected pilot provides an instantaneous frequency reference that remains valid until the accumulated Doppler drift exceeds the symbol tolerance. Consequently, the pilot density must scale with the Doppler variation rate. By analyzing the Doppler distribution across the satellite beam footprint from a satellite-centric perspective (Fig. 9b), we identify near-zenith (90°-elevation-angle) passes as the worst-case scenario, as they exhibit the largest Doppler-time gradients. Accordingly, *CommSAR* configures the pilot density based on this most stringent requirement, ensuring reliable demodulation across all overpass geometries. Since the Doppler evolution of a satellite in a stable orbit is almost deterministic, this density can be pre-configured offline, thereby eliminating real-time onboard computational overhead.

D-BPSK as a Phase-Rotation Anchor. In the uplink, the rapid satellite motion (up to $\pm 8.5 \times 10^7$ deg/s) and the discontinuous nature of radar pulses preclude coherent demodulation due to the lack of a stable phase reference. However, as the channel remains quasi-static over μs-scale symbol intervals, *CommSAR* adopts D-BPSK. By detecting the relative phase difference between adjacent symbols, the system inherently cancels out the mobility-induced phase rotation. This mechanism enables reliable blind demodulation without the need for complex phase tracking.

4 Implementation

In this section, we present the detailed implementation of *CommSAR*'s SAR radar and GS prototypes.

***CommSAR* Radar Prototypes.** We implement *CommSAR* imaging radar prototypes using the FPGA-based direct digital synthesizer (DDS) architecture [42], which is the prevailing waveform generation architecture in commercial SAR satellites [1, 10, 11, 51]. DDS is a digitally sampled waveform generator driven by a high-stability clock, enabling flexible generation of arbitrary transmit waveforms defined by software. Leveraging this programmability, *CommSAR* functionality is enabled solely through FPGA firmware updates, requiring no modifications to the RF front-end, analog signal chain, or other hardware. As a result, existing SAR radars can be directly upgraded to support *CommSAR* without any hardware changes.

Table 1: FPGA firmware upgrade from SAR to *CommSAR* on the same FPGA hardware as the in-orbit satellite testbed.

	***CommSAR* upgrade over SAR**	**Added overhead**
Code	Changed in waveform-generation module: add CS-LFM waveform-generation logic that maps data symbols to cyclic DDS read-pointer offsets.	+400 lines of code (≈1.5%)
	Other modules unchanged: clock/reset, ADC/DAC interfaces, timing/RF control, acquisition/processing, frame packing/storage, and NAND control.	0
Runtime	Increased in lookup tables (LUTs): added waveform-control logic uses more programmable logic.	+708 LUTs (≈1.3%)
	Increased in block RAMs (BRAMs): extra on-chip buffer memory is allocated within the CS-LFM waveform-generation path.	+39 BRAMs (≈8.3%)
	Other runtime resources show no increase: flip-flops (FFs), LUT RAMs, DSP slices, I/O pins, gigabit transceivers (GTs), global clock buffers (BUFGs), and mixed-mode clock managers (MMCMs).	0

Table 1 summarizes the satellite-side firmware delta. *CommSAR* modifies only the waveform-generation module, adding about 400 Verilog lines to a 27K-line SAR FPGA program (≈1.5%). After full resynthesis, the only increased FPGA resources are LUTs, from 54,874 to 55,582 (+708, ≈1.3%), and BRAMs, from 470.5 to 509.5 (+39, ≈8.3%). Resource utilization for LUT RAMs, FFs, DSP slices, I/O pins, GTs, BUFGs, and MMCMs remains unchanged.

However, due to limited operational permissions granted by our industrial partner, we are unable to directly modify the firmware on the in-orbit commercial satellite at this stage, as shown in Fig. 10. Instead, we are limited to measuring the communication channel and collecting the corresponding SAR imaging outputs. To overcome this practical constraint while fully leveraging the existing in-orbit satellite resources, we implement two DDS-based *CommSAR* radar prototypes: (1) an anechoic-chamber-mounted COTS SAR radar (as shown in Fig. 11a) operating in the X-band, which is *the same model as the in-orbit satellite*, and (2) a UAV-mounted COTS SAR radar (Fig. 11b) operating in the Ka-band, which is lightweight enough to be carried by a UAV. We jointly use these radar prototypes running *CommSAR* firmware to evaluate each module of *CommSAR*, with the detailed methodology described in Sec. 5.1.

***CommSAR* GS Prototypes.** We develop the *CommSAR* GS prototypes (Fig. 11c) for bidirectional communication experiments. For downlink reception, we employ a horn antenna integrated with a tunable downconverter and a computer-based demodulator. For uplink signal modulation, we fabricate the programmable metasurfaces tailored to two specific radar platforms: a 30×30 Ka-band array for the UAV-based prototype and a 60×60 X-band array for the in-orbit satellite. The fabricated metasurfaces are shown in Fig. 16 in the Appendix. To support different radar bands, the GS simply replaces the horn antenna and metasurface with wavelength-specific counterparts. The metasurface retains the same programmable unit-cell topology and control interface, while the horn preserves the same antenna geometry; only the physical dimensions of both components are scaled to the target wavelength. All metasurface unit cells are controlled by a shared control signal generated by an

Arduino. The downlink receiver exports the detected pulse-onset signal as a hardware trigger to the Arduino controller, which immediately initiates the preloaded metasurface switching sequence. Compared with conventional designs, the proposed GS prototype is significantly more compact, portable, and easier to deploy.

5 Evaluation

In this section, we first describe the evaluation methodology. We then present the corresponding results and analysis for the downlink and uplink, respectively.

5.1 Methodology

To fully leverage existing in-orbit satellite resources while thoroughly evaluating each module of *CommSAR*, we design the following evaluation methodology, experimental setup, and metrics.

Downlink Impact on Imaging. Since the CS-LFM waveform cannot be directly deployed on our in-orbit commercial satellite, we implement it on the UAV-mounted *CommSAR* radar prototype (as shown in Fig. 11b) to evaluate downlink-induced impact on imaging. The UAV flies at an altitude of 300 m with a constant velocity of 5 m/s, enabling the formation of a synthetic aperture analogous to that of a SAR satellite. By alternating between CS-LFM and standard LFM waveforms across successive pulse windows, we compare *CommSAR* with conventional SAR imaging under identical scenes, flight conditions, and radar hardware. For quantitative evaluation, we use *resolution*, *peak sidelobe ratio (PSLR)*, and *integrated sidelobe ratio (ISLR)* to characterize the point-target impulse response. It should be noted that the UAV is used solely for the imaging evaluation (*i.e.*, LFM vs. CS-LFM comparison) and is not involved in any subsequent communication-related experiments.

Downlink Communication Performance. Although the CS-LFM waveform cannot be directly deployed on the existing in-orbit satellite, we can still measure the real downlink channel under actual satellite motion, propagation conditions, and RF impairments based on our in-orbit satellite and GS. We then generate the proposed CS-LFM waveform using the same FPGA-based DDS radar (Fig. 11a) employed by the in-orbit satellite and incorporate the measured downlink channel response into the transmitted signal. To further eliminate external interference and environmental effects, the experiment is conducted in a microwave anechoic chamber. We use the uncoded physical-layer *bit error rate* (BER) to evaluate downlink communication performance under different channel conditions. Unless otherwise noted, the SNR reported in all communication BER plots refers to the raw sample-level SNR before dechirping, symbol integration, and decoding. Since each CS-LFM symbol encodes m bits, downlink BER is computed based on the Hamming distance between the decoded and transmitted m-bit symbol indices, normalized by the total number of transmitted bits.

Uplink Imaging Impact and Communication Performance. We obtain onboard IQ traces of echoes reflected by our ground-deployed metasurfaces and recorded by the in-orbit satellite; these traces are used to evaluate uplink communication performance and its impact on imaging. The detailed orbital info of the satellite is shown in Fig. 10. To assess the uplink impact on imaging, since the proposed echo-based shared-waveform uplink affects only the GS resolution cell, corresponding to one or a few pixels in the SAR image, we present the resulting SAR images without quantitative analysis. For uplink communication performance, we use the uncoded physical-layer BER computed over the D-BPSK payload bits. Barker symbols are used solely for synchronization and are excluded from the payload, while a synchronization failure causes all payload bits in the corresponding pulse to be counted as erroneous.

Table 2: Quantitative comparison of point-target imaging metrics between SAR and *CommSAR*. For each metric, the better value is highlighted in bold.

Flight	Direction	Resolution (m)		PSLR (dB)		ISLR (dB)	
		SAR	*CommSAR*	SAR	*CommSAR*	SAR	*CommSAR*
#1	Azimuth	**0.1064**	0.1106	**-15.2217**	-14.7790	**-12.0493**	-11.9901
	Range	0.1843	**0.1766**	**-14.6180**	-14.3928	**-13.1985**	-11.6186
#2	Azimuth	0.1079	**0.1041**	-16.5228	**-16.6590**	-13.0646	**-13.2310**
	Range	0.1827	**0.1788**	**-20.1172**	-19.0233	**-16.2049**	-15.4610
#3	Azimuth	**0.0846**	0.0852	-14.0381	**-14.0468**	**-11.0188**	-10.1511
	Range	0.1942	**0.1711**	-16.6492	**-18.2162**	**-14.7511**	-13.9108

5.2 Downlink Impact on Imaging

We evaluate the impact of *CommSAR* downlink modulation on SAR imaging quality using the UAV-based radar prototype. Since UAV trajectories are less repeatable than satellite orbits, we avoid comparing two independent flights. Instead, the radar transmits CS-LFM and standard LFM pulses in an interleaved manner: odd pulses use the *CommSAR* waveform, while even pulses use the conventional SAR waveform. This design ensures that the two waveforms share almost the same radar hardware, platform trajectory, synthetic aperture geometry, scene, and propagation environment. After data collection, the received echoes are de-interleaved into CS-LFM and standard LFM subsets, which are then processed independently by the *CommSAR* and conventional SAR imaging pipelines, respectively. The evaluation is conducted in two stages: (1) a qualitative visual comparison at the scene level and (2) a quantitative point-target impulse-response assessment.

Cross-Platform Fidelity. This experiment does not attempt to reproduce the exact satellite imaging geometry. Instead, it verifies the key waveform-level question: whether CS-LFM can achieve the same SAR focusing behavior as standard LFM when both waveforms observe the same scene through the same aperture, hardware, trajectory, and imaging SNR. The transition from the UAV prototype to the satellite platform changes parameters such as range, velocity, carrier frequency, and Doppler history. However, these are standard platform-dependent inputs to SAR focusing algorithms [2, 8, 31] and are matched accordingly for both CS-LFM and LFM processing. Therefore, they do not introduce any additional imaging penalty specific to CS-LFM. The only remaining waveform-specific factor is pulse compression under matched filtering, which is analyzed in Sec. 3.1 and empirically validated through the interleaved A/B test. This is also consistent with the common practice of validating SAR imaging waveforms and processing algorithms using airborne experiments before spaceborne deployment [34, 35].

Visual Scene-Level Comparison. We conduct three UAV flights using modulation orders of 8 bits, 9 bits, and 10 bits, corresponding to low, medium, and high modulation orders, respectively. Fig. 12 compares the conventional SAR and *CommSAR* imaging results across all three flights. The scenes cover diverse land-cover types

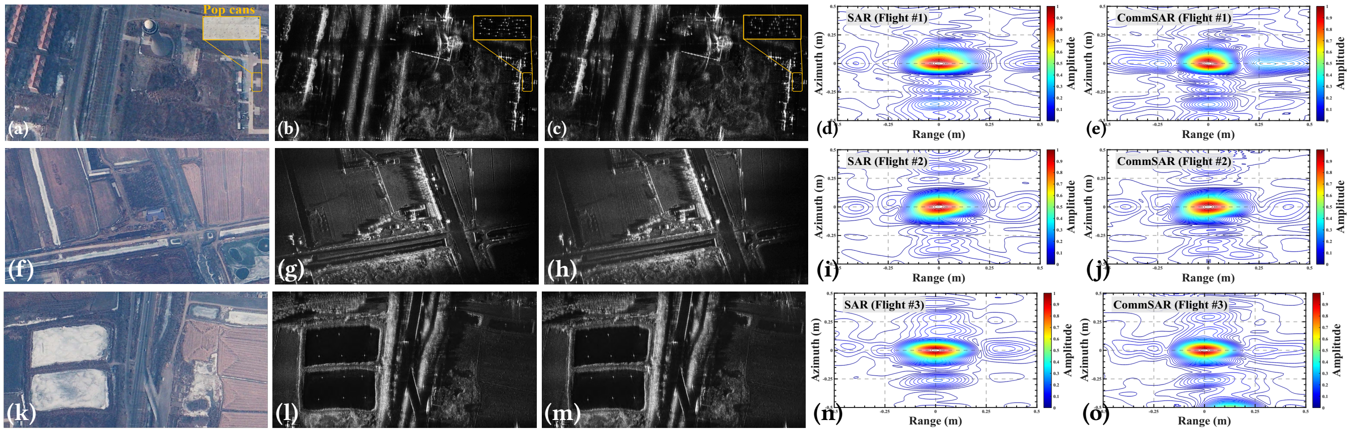

Figure 12: Visual comparison of standard SAR (LFM) and *CommSAR* (CS-LFM) imaging results across three real UAV flights (rows). Columns correspond to: (a, f, k) Optical reference (Google Maps); (b, g, l) Standard SAR imaging; (c, h, m) *CommSAR* imaging; (d, i, n) Standard SAR point-target response, and (e, j, o) *CommSAR* point-target response. The bright pattern spelling "SAR" at the upper-right of (a, b, c) is formed by pop cans spaced ≈1.5 m apart; their strong metallic reflections act as point scatterers, revealing the spatial resolution. Across all flights, *CommSAR* preserves imaging fidelity with no visible artifacts. Full resolution SAR/*CommSAR* images of this experiment can be found in Appendix B.

and scattering structures, including farmland, asphalt roads, concrete and brick buildings, metallic towers, and water bodies such as ponds. Across all modulation orders, the *CommSAR* images exhibit visual quality comparable to that of conventional SAR images. Major scene structures, dominant scatterers, and spatial layouts are well preserved, including compact metallic scatterers, linear road features, field and water boundaries, and building and land-cover patterns that support common SAR interpretation tasks. We observe no noticeable artifacts or geometric distortions as the modulation order increases, indicating that CS-LFM modulation does not visibly remove or distort application-relevant image cues.

Point-Target Impulse Response Analysis. While a visual scene-level comparison evaluates overall image fidelity, point-target analysis offers a more sensitive evaluation of the radar system's impulse response characteristics. We perform point-target analysis using isolated strong scatterers extracted from the reconstructed images, as illustrated in the six rightmost subfigures of Fig. 12. For each modulation order, we evaluate resolution, peak sidelobe ratio (PSLR), and integrated sidelobe ratio (ISLR) in both azimuth and range dimensions. Table 2 compares the point-target metrics between SAR and *CommSAR*. Across all modulation orders, *CommSAR* achieves resolutions that are comparable to, and in several cases slightly better than, those of standard SAR. PSLR and ISLR values remain on par with conventional SAR. Moreover, we observe no systematic degradation as the modulation order increases. This behavior is expected, as the CS-LFM waveform is theoretically transparent to the SAR imaging process, as analyzed in Sec. 3.1.

5.3 Downlink Communication

Using the real-channel-data–assisted methodology described above, we evaluate the performance of CS-LFM downlink communication under various SNR levels and Doppler shifts measured from the real satellite-to-ground channel. We further evaluate the throughput degradation introduced by the proposed pilot insertion scheme used to combat extreme satellite mobility.

Impact of SNR. We evaluate the uncoded physical-layer BER of the proposed CS-LFM scheme under varying SNRs encountered as the satellite passes over our GS. We use the recorded channel noise from the real satellite-to-ground link as the baseline noise and synthesize additional additive white Gaussian noise to systematically reduce the SNR. We test different modulation orders m (where each CS-LFM symbol encodes m bits) and the corresponding results are shown in Fig. 13a. The BER results reveal a fundamental trade-off between spectral efficiency and noise robustness: increasing m packs more CS-LFM symbols into the same bandwidth but reduces the tolerance margin against noise. However, even at the maximum bandwidth-limited modulation order of $m = 13$, the downlink BER falls below 10^{-3} once the SNR reaches approximately 15 dB. Notably, our real-world measurements from the in-orbit SAR satellite show that the minimum received SNR is approximately 18 dB, even at a low elevation angle of 30°. This establishes a link margin of approximately 3 dB over the 10^{-3} BER operating point.

Impact of Doppler Shifts. Doppler shifts pose a critical challenge to CS-LFM demodulation because they introduce frequency offsets that can lead to incorrect symbol decisions and, consequently, bit errors. To isolate the impact of Doppler shifts, we fix the baseline SNR to the minimum value observed in the real satellite–ground channel, which is 18 dB. Fig. 13b illustrates the diverse time-varying downlink Doppler shifts during satellite passes with different maximum elevation angles, based on our in-orbit satellite. To quantify the inherent sensitivity of CS-LFM to these shifts, we evaluate the uncoded physical-layer BER as a function of Doppler shift with the opposite-slope LFM pilot-based compensation *disabled*. The results, shown in Fig. 13c, reveal that sensitivity to Doppler shifts scales with the modulation order m. By cross-referencing these results with Fig. 13a—where the same modulation order ($m = 13$) remains below the plotted BER range at 18 dB SNR with pilot compensation enabled—the comparison shows that pilot insertion is essential for reliable high-order downlink demodulation under satellite-induced Doppler shifts across realistic overpass geometries.

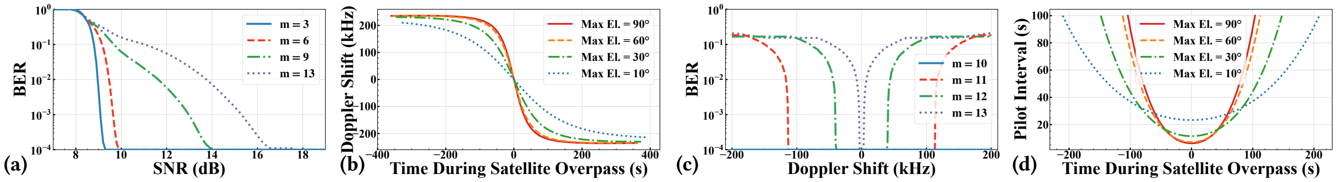

Figure 13: Evaluation of *CommSAR* downlink communication performance.

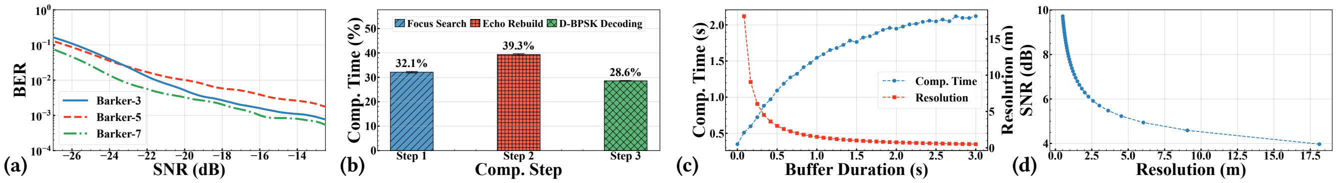

Figure 14: *CommSAR* uplink communication evaluation.

Figure 15: In-orbit SAR image acquired during *CommSAR* uplink communication.

Throughput Overhead of Pilot Insertion. Given the effectiveness of the proposed pilot insertion scheme, we further quantify the throughput degradation introduced by this design. With the measured Doppler shifts in Fig. 13b, we calculate the corresponding maximum allowable pilot insertion interval, as illustrated in Fig. 13d. This interval is determined by requiring the Doppler drift between consecutive pilots to remain below half of the CS-LFM symbol spacing, ensuring that the residual frequency offset does not cross the nearest symbol decision boundary. As expected, the Doppler drift depends strongly on the satellite's elevation angle during the pass, with the 90° near-zenith pass representing the worst-case scenario. Notably, even in this most demanding near-zenith scenario, the derived maximum allowable pilot interval for our CS-LFM modulation scheme remains above 5 seconds, indicating that only infrequent pilot insertion is required. With one pilot pulse inserted every five seconds, the fraction of pulses used for CS-LFM data transmission is $\frac{f_{\text{PRF}}-1/5}{f_{\text{PRF}}}$, which yields 99.9975% at the maximum PRF (f_{PRF}=8000). Hence, the 5 s pilot strategy ensures robust Doppler compensation while introducing a negligible throughput overhead.

5.4 Uplink Performance

We evaluate *CommSAR*'s uplink directly with the in-orbit SAR satellite, preserving the real satellite-ground geometry, propagation channel, and RF hardware conditions. The uplink evaluation focuses on three aspects: (1) the visual scene-level impact of the modulated uplink waveforms; (2) the communication reliability of the metasurface-based uplink; and (3) the computational overhead of uplink demodulation.

Visual Scene-Level Results. Fig. 15 shows the in-orbit SAR image acquired during uplink communication. Because the metasurface acts as a dedicated point scatterer, standard SAR processing focuses its modulated echo into the GS's resolution cell. Consequently, the visual impact of the uplink transmission is inherently confined to the GS's geolocation cell (*i.e.*, only a few bright pixels), while the rest of the scene remains unchanged. This visualization also illustrates the spatial filtering underlying uplink demodulation: the standard SAR focusing process naturally separates the metasurface echo from the surrounding scene clutter.

Uplink Communication Reliability. Although the in-orbit satellite transmits standard LFM pulses instead of CS-LFM, the uplink demodulator recovers only the residual phase between the metasurface echo and the known transmitted chirp, rather than the absolute chirp phase. Consequently, the standard-LFM experiment is representative of CS-LFM uplink operation: in both cases, matched dechirping removes the deterministic chirp phase, leaving only the D-BPSK phase imposed by the metasurface. The uplink uses D-BPSK with a 14-symbol intra-pulse modulation sequence, where a Barker preamble provides symbol synchronization. To stress-test link reliability, we inject controlled noise into the real satellite echoes and vary both the SNR and Barker-code length. Fig. 14a reports the end-to-end uplink BER over payload bits. This metric includes both Barker synchronization failures and D-BPSK payload errors after successful synchronization: Barker symbols are not counted as payload, while a synchronization failure causes all payload bits in that pulse to be counted as erroneous.

Barker-3 reaches the 10^{-3} BER target at about -13 dB SNR, showing that a short synchronization sequence is already sufficient in our measured traces. Longer Barker sequences do not provide a consistent BER reduction, suggesting that the residual errors in this regime are not dominated solely by synchronization failures. Since increasing the Barker length also reduces the number of payload symbols per pulse, from 11 with Barker-3 to 9 and 7 with Barker-5 and Barker-7, respectively, we use Barker-3 as the default operating point because it provides a favorable rate–robustness trade-off.

Computational Overhead of Uplink Demodulation. For uplink demodulation, *CommSAR* reuses standard SAR focusing as the spatial-filtering primitive and runs a communication-specific demodulation path in three stages: (1) *Focus Search*, whose latency is dominated by the standard SAR focusing process; once the image is focused, locating the metasurface cell is a simple crop using the known GS geolocation; (2) *Echo Rebuild*, which applies inverse focusing to recover a clutter-suppressed time-domain echo; and (3) *D-BPSK Decoding*, which dechirps and differentially demodulates the recovered echo. Fig. 14b reports this latency breakdown: the first bar corresponds to the focusing-dominated focus search stage, while the other two correspond to the echo rebuild and D-BPSK decoding stages.

We then vary the focusing buffer duration, which is the primary parameter that trades latency for spatial selectivity. Longer buffers improve azimuth resolution, allowing the extracted cell to contain less surrounding clutter and achieve a higher rebuilt-echo SNR (Fig. 14d). However, the same buffers require processing more pulses, thereby increasing computation time (Fig. 14c). Together, these results quantify how buffer duration trades computational latency for rebuilt-echo SNR, allowing *CommSAR* to choose a buffer duration based on the required link margin and latency budget.

6 Discussion

This section discusses the capabilities enabled by higher TT&C rates, the SAR imaging modes best suited for *CommSAR*, and the implications of shared-waveform TT&C for control-plane security.

Higher TT&C Rates. A 100-kbps-class TT&C link does more than satisfy conventional requirements: it substantially expands the amount of control-plane data that can be exchanged within a short contact window. Conventional TT&C baselines require at least 2 kbps for telecommand and 9.6 kbps for telemetry [21], while *CommSAR* provides a bidirectional link on the order of 100 kbps. This rate headroom enables more agile SAR operations, including MB-scale on-orbit updates for new imaging modes or onboard processing models, as well as rapid transmission of quick-look previews from newly acquired SAR scenes. Such previews allow operators to assess acquisition quality and issue follow-up commands within the same contact window or the next available contact.

SAR-Mode Scope. *CommSAR* is mode-dependent because SAR modes differ in dwell time, beam geometry, and SNR. It is best matched to high-resolution spotlight variants, where beam steering prolongs GS illumination and provides the SNR margin needed for shared-waveform communication. These modes further support the fine-resolution, target-centric imaging increasingly adopted by agile commercial SAR systems [5, 13, 14, 44]. Stripmap, ScanSAR, and other wide-swath modes are not excluded; however, their shorter dwell times or less optimal illumination geometries may reduce the available SNR and contact duration.

Security and Control-Plane Coupling. *CommSAR* integrates TT&C with the SAR sensing waveform only at the physical layer and is not intended to replace conventional TT&C security mechanisms. As in legacy TT&C links, confidentiality, integrity, authentication, and anti-replay protection should be enforced at higher protocol layers above the waveform [6, 7, 24]. Thus, eavesdroppers can access only cryptographically protected bits, while forged commands are rejected without valid authentication. The primary residual risk is availability: jamming or disruption of the SAR waveform can simultaneously degrade the embedded control channel. Mitigation methods, such as frequency agility and operational scheduling, remain system-level considerations, while a comprehensive anti-jamming design is beyond the scope of this paper.

7 Related Work

In this section, we review related work on LEO satellite communication from two perspectives: systems that use dedicated communication links and systems that reuse existing signal resources.

LEO Communication over Dedicated Links. Both academia and industry have made significant advances in LEO communication links. Academic work spans broadband constellations and downlink architectures [16, 47], low-cost GS access [27, 39], narrowband satellite-IoT [32, 38, 52], and direct-to-satellite cellular connectivity [18]. Despite their different settings, these efforts still optimize conventional TT&C, payload-data, or service links, rather than departing from the dedicated-link paradigm by reusing onboard sensing signals. Industry systems, on the other hand, extend contact time through inter-satellite laser meshes, as in Starlink [23], or MEO/GEO relay infrastructure such as TDRSS- and EDRS-like systems [12, 25]. While these systems can provide additional ground access for future satellites, they require additional spaceborne hardware, such as optical terminals [41], and therefore cannot be retrofitted to the more than 200 LEO SAR satellites already in orbit.

Communication over Existing Radar Signals. Most ISAC designs for radar waveforms target terrestrial radar [17, 40, 54]. They either add signals/protocol steps to the pulses [19] or alter waveform parameters [26], both of which disturb SAR imaging, which depends on pulse compression and aperture focusing. For SAR satellites specifically, *downlink-oriented designs* embed communication into the sensing waveform by splitting the chirp and data across disjoint OFDM subcarriers [49] or transmitting communication-centric waveforms [20, 22, 53], both of which degrade imaging quality. *Uplink-oriented designs* rely on RCS-modulated reflectors [9] or code-domain backscatter signatures spread across many PRIs [29], both of which suffer from low data rates. Moreover, to the best of our knowledge, no existing work provides bidirectional TT&C links. *CommSAR* instead pushes the Pareto frontier by using the native SAR waveform as a *bidirectional* carrier.

8 Conclusion

This paper introduces *CommSAR*, a bidirectional framework enabling satellite-ground communication via native SAR pulses and echoes. Its primary advantage lies in facilitating robust data exchange without requiring hardware modifications to existing SAR satellites. On the ground, *CommSAR* combines a compact reflective metasurface with a small-form-factor antenna to enable miniaturized GSs that achieve bidirectional communication rates exceeding 100 kbps. This infrastructure-lean approach lowers deployment barriers and shifts satellite–ground integration from bulky fixed GSs toward resilient portable terminals, ensuring that mission-critical TT&C operations remain accessible anytime and anywhere.

9 Acknowledgments

We thank our shepherd and the anonymous reviewers for their insightful comments. This work is supported in part by the NSFC (No. U25B2037, W2412089), the Start-up funding for the School of Computer Science, SJTU (No. WH220403302), and the NTU SUG-NAP (No. 024859-00001).

References

[1] Jinhong An, Haewon Jung, Heein Yang, Sang-Burm Ryu, Hyeon-Cheol Lee, Sang-Gyu Lee, Sang-Soon Yong, and Jae-Hyun Kim. 2015. Development of Chirp Signal Generator for Micro Satellite On-board Synthetic Aperture Radar. In *IEEE International Geoscience and Remote Sensing Symposium (IGARSS)*. 3663–3666. doi:10.1109/IGARSS.2015.7326617

[2] Richard Bamler. 1992. A Comparison of Range-Doppler and Wavenumber Domain SAR Focusing Algorithms. *IEEE Transactions on Geoscience and Remote Sensing (TGRS)* 30, 4 (1992), 706–713. doi:10.1109/36.158864

[3] Peter Borwein and Michael J. Mossinghoff. 2014. Wieferich Pairs and Barker Sequences, II. *LMS Journal of Computation and Mathematics* 17, 1 (2014), 24–32. doi:10.1112/S1461157013000223

[4] Ciro Cafforio, Claudio Maria Prati, and Fabio Rocca. 1991. SAR Data Focusing Using Seismic Migration Techniques. *IEEE Transactions on Aerospace and Electronic Systems (TAES)* 27, 2 (1991), 194–207. doi:10.1109/7.78293

[5] Capella Space. 2026. What are Capella's collect modes? https://support.capellaspace.com/what-are-capellas-collect-modes.

[6] Consultative Committee for Space Data Systems. 2022. *Space Data Link Security Protocol*. Technical Report CCSDS 355.0-B-2. Consultative Committee for Space Data Systems.

[7] Consultative Committee for Space Data Systems. 2024. *Space Data Link Security Protocol—Summary of Concept and Rationale*. Technical Report CCSDS 350.5-G-2. Consultative Committee for Space Data Systems.

[8] John C Curlander and Robert N McDonough. 1991. *Synthetic Aperture Radar: Systems and Signal Processing*. Wiley.

[9] Geneva Ecola, Bill Yen, Ana Banzer Morgado, Bodhi Priyantha, Ranveer Chandra, and Zerina Kapetanovic. 2025. SARLink: Satellite Backscatter Connectivity using Synthetic Aperture Radar. In *ACM SenSys*. ACM, 398–410. doi:10.1145/3715014.3722061

[10] Edwar and Achmad Munir. 2015. Development of SAR Transmitter for Nanosatellite-based Remote Sensing Application. In *IEEE ICEEI*. 318–321. doi:10.1109/ICEEI.2015.7352518

[11] Edwar and Achmad Munir. 2018. Prototype of Dual DDS FMCW Transmitter for L-band Synthetic Aperture Radar. *Journal of Measurements, Electronics, Communications, and Systems* 4, 1 (2018), 8–15. doi:10.25124/jmecs.v4i1.1694

[12] European Space Agency. 2026. European Data Relay System: Infrastructure. https://www.esa.int/Applications/Connectivity_and_Secure_Communications/EDRS/Infrastructure.

[13] Nan Ge, Fernando Rodriguez Gonzalez, Yuanyuan Wang, Yilei Shi, and Xiao Xiang Zhu. 2018. Spaceborne Staring Spotlight SAR Tomography—A First Demonstration With TerraSAR-X. *IEEE Journal of Selected Topics in Applied Earth Observations and Remote Sensing* 11, 10 (2018), 3743–3756. doi:10.1109/JSTARS.2018.2851752

[14] ICEYE. 2026. Imaging Modes. https://www.iceye.com/sar-data/imaging-modes.

[15] Thomas Sean Kelso. 2023. CelesTrak: Two-Line Element Set Format. https://celestrak.org/columns/v04n03.

[16] Yuanjie Li, Hewu Li, Wei Liu, Lixin Liu, Wei Zhao, Yimei Chen, Jianping Wu, Qian Wu, Jun Liu, Zeqi Lai, and Han Qiu. 2023. A Networking Perspective on Starlink's Self-Driving LEO Mega-Constellation. In *ACM MobiCom*. Madrid, Spain. doi:10.1145/3570361.3592519

[17] Fan Liu, Yuanhao Cui, Christos Masouros, Jie Xu, Tony Xiao Han, Yonina C Eldar, and Stefano Buzzi. 2022. Integrated Sensing and Communications: Toward Dual-functional Wireless Networks for 6G and Beyond. *IEEE Journal on Selected Areas in Communications (JSAC)* 40, 6 (2022), 1728–1767. doi:10.1109/JSAC.2022.3156632

[18] Wei Liu, Yuanjie Li, Jingyi Lan, Hewu Li, Yimei Chen, Lixin Liu, Jiabo Yang, Xi Long, Li Ouyang, Minghao Tang, Jianping Wu, Qian Wu, Jun Liu, and Zeqi Lai. 2025. Direct-to-Cell Satellite Network without Satellite Navigation. In *ACM SIGCOMM*. Coimbra, Portugal. doi:10.1145/3718958.3750522

[19] Haofan Lu, Mohammad Mazaheri, Reza Rezvani, and Omid Abari. 2023. A Millimeter Wave Backscatter Network for Two-Way Communication and Localization. In *ACM SIGCOMM*. ACM, 49–61. doi:10.1145/3603269.3604873

[20] Marco Manzoni, Stefano Moro, Francesco Linsalata, Mattia Giovanni Polisano, Andrea Virgilio Monti-Guarnieri, and Stefano Tebaldini. 2024. Evaluation of UAV-Based ISAC SAR Imaging: Methods and Performances. In *IEEE RadarConf*. 1–6. doi:10.1109/RadarConf2458775.2024.10548165

[21] Dwayne R. Morgan, Ron G. Streich, Barton Bull, Chuck Grant, and Edward I. Power. 2001. Telemetry Tracking & Control (TT&C) - first TDRSS, then Commercial GEO & Big LEO and Now Through LEO. In *International Symposium on Reducing Cost of Spacecraft Ground System and Operations*. https://ntrs.nasa.gov/citations/20010027550

[22] Stefano Moro, Francesco Linsalata, Marco Manzoni, Maurizio Magarini, and Stefano Tebaldini. 2024. Exploring ISAC Technology for UAV SAR Imaging. In *IEEE ICC*. IEEE, 1582–1587. doi:10.1109/ICC51166.2024.10622910

[23] Muon Space. 2025. Muon Space to Integrate SpaceX's Starlink Mini Space Lasers Into Its Halo Satellite Platform. https://www.muonspace.com/press/muon-space-to-integrate-spacexs-starlink-mini-space-lasers-into-its-halo-tm-satellite-platform.

[24] National Aeronautics and Space Administration. 2022. *Space System Protection Standard*. Technical Report NASA-STD-1006A. NASA Technical Standards System.

[25] National Aeronautics and Space Administration. 2026. Tracking and Data Relay Satellites (TDRS). https://www.nasa.gov/missions/tdrs/tracking-and-data-relay-satellite-tdrs-generations-of-spacecraft/.

[26] Ryu Okubo, Luke Jacobs, Jinhua Wang, Steven Bowers, and Elahe Soltanaghai. 2024. Integrated Two-way Radar Backscatter Communication and Sensing with Low-power IoT Tags. In *ACM SIGCOMM*. ACM, 327–339. doi:10.1145/3651890.3672226

[27] Hao Pan, Lili Qiu, Bei Ouyang, Shicheng Zheng, Yongzhao Zhang, Yi-Chao Chen, and Guangtao Xue. 2023. PMSat: Optimizing Passive Metasurface for Low Earth Orbit Satellite Communication. In *ACM MobiCom*. Madrid, Spain. doi:10.1145/3570361.3613257

[28] John B. Pendry, Anthony J. Holden, D. J. Robbins, and William J. Stewart. 1999. Magnetism from Conductors and Enhanced Nonlinear Phenomena. *IEEE Transactions on Microwave Theory and Techniques (TMTT)* 47, 11 (1999), 2075–2084. doi:10.1109/22.798002

[29] Alex Piccioni, Roberto Alesii, Fortunato Santucci, and Fabio Graziosi. 2025. A Testing Framework for Joint Communication and Sensing in Synthetic Aperture Radars. *IEEE Access* (2025). doi:10.1109/ACCESS.2025.3531328

[30] Danielle Racelis and Mathieu Joerger. 2018. High-integrity TLE Error Models for MEO and GEO Satellites. In *AIAA SPACE and Astronautics Forum and Exposition*. 5241. doi:10.2514/6.2018-5241

[31] Russell Keith Raney, Hartmut Runge, Richard Bamler, Ian G. Cumming, and Frank H. Wong. 1994. Precision SAR Processing Using Chirp Scaling. *IEEE Transactions on Geoscience and Remote Sensing (TGRS)* 32, 4 (1994), 786–799. doi:10.1109/36.298008

[32] Yidong Ren, Amalinda Gamage, Li Liu, Mo Li, Shigang Chen, Younsuk Dong, and Zhichao Cao. 2024. SateRIoT: High-performance Ground-Space Networking for Rural IoT. In *ACM MobiCom*. Washington, DC, USA. doi:10.1145/3636534.3690659

[33] Kathleen Riesing. 2015. Orbit Determination from Two Line Element Sets of ISS-deployed Cubesats. In *29th Annual AIAA/USU Conference on Small Satellites*. Logan, UT, USA. https://digitalcommons.usu.edu/smallsat/2015/all2015/58/

[34] Rafael F. Rincon, Manuel A. Vega, Manuel Buenfil, Alessandro Geist, Lawrence Hilliard, and Paul Racette. 2011. NASA's L-Band Digital Beamforming Synthetic Aperture Radar. *IEEE Transactions on Geoscience and Remote Sensing (TGRS)* 49, 10 (2011), 3622–3628. doi:10.1109/TGRS.2011.2157971

[35] Marc Rodriguez-Cassola, Stefan V. Baumgartner, Gerhard Krieger, and Alberto Moreira. 2010. Bistatic TerraSAR-X/F-SAR Spaceborne-Airborne SAR Experiment: Description, Data Processing and Results. *IEEE Transactions on Geoscience and Remote Sensing (TGRS)* 48, 2 (2010), 781–794. doi:10.1109/TGRS.2009.2029984

[36] satellitemap.space. 2025. Find Starlink Satellites. https://satellitemap.space/constellation/starlink.

[37] Semtech. 2024. What are LoRa and LoRaWAN. https://lora-developers.semtech.com/documentation/tech-papers-and-guides/lora-and-lorawan.

[38] Jayanth Shenoy, Om Chabra, Tusher Chakraborty, Suraj Jog, Deepak Vasisht, and Ranveer Chandra. 2024. CosMAC: Constellation-Aware Medium Access and Scheduling for IoT Satellites. In *ACM MobiCom*. Washington, DC, USA. doi:10.1145/3636534.3690657

[39] Vaibhav Singh, Akarsh Prabhakara, Diana Zhang, Osman Yagan, and Swarun Kumar. 2021. A Community-Driven Approach to Democratize Access to Satellite Ground Stations. In *ACM MobiCom*. New Orleans, LA, USA. doi:10.1145/3447993.3448630

[40] Christian Sturm and Werner Wiesbeck. 2011. Waveform Design and Signal Processing Aspects for Fusion of Wireless Communications and Radar Sensing. *Proc. IEEE* 99, 7 (2011), 1236–1259. doi:10.1109/JPROC.2011.2131110

[41] Tesat-Spacecom GmbH & Co. KG. 2026. Products. https://www.tesat.de/products.

[42] Joseph Tierney, Charles M. Rader, and Bernard Gold. 1971. A Digital Frequency Synthesizer. *IEEE Transactions on Audio and Electroacoustics* 19, 1 (1971), 48–57. doi:10.1109/TAU.1971.1162151

[43] Lars M. H. Ulander, Hans Hellsten, and Gunnar Stenstrom. 2003. Synthetic-Aperture Radar Processing Using Fast Factorized Back-projection. *IEEE Transactions on Aerospace and Electronic Systems (TAES)* 39, 3 (2003), 760–776. doi:10.1109/TAES.2003.1238734

[44] Umbra Lab Inc. 2026. Spotlight Mode. https://umbra.space/remote-sensing/spotlight/.

[45] Union of Concerned Scientists. 2023. UCS Satellite Database. https://www.ucs.org/resources/satellite-database.

[46] David Vallado and Paul Crawford. 2008. SGP4 Orbit Determination. In *AIAA/AAS Astrodynamics Specialist Conference and Exhibit*. Honolulu, HI, USA. doi:10.2514/6.2008-6770

[47] Deepak Vasisht, Jayanth Shenoy, and Ranveer Chandra. 2021. L2D2: Low Latency Distributed Downlink for Low Earth Orbit Satellites. In *ACM SIGCOMM*. Virtual Event, USA. doi:10.1145/3452296.3472932

[48] Jack L. Walker. 1980. Range-Doppler Imaging of Rotating Objects. *IEEE Transactions on Aerospace and Electronic Systems (TAES)* AES-16, 1 (1980), 23–52. doi:10.1109/TAES.1980.308875

[49] Jie Wang, Xing-Dong Liang, Long-Yong Chen, Li-Na Wang, and Kun Li. 2019. First Demonstration of Joint Wireless Communication and High-Resolution SAR Imaging Using Airborne MIMO Radar System. *IEEE Transactions on Geoscience and Remote Sensing (TGRS)* 57, 9 (2019), 6619–6632. doi:10.1109/TGRS.2019.2907561

[50] Baolong Wu, Chengjin Liu, and Jianlai Chen. 2024. A Review of Spaceborne High-Resolution Spotlight/Sliding Spotlight Mode SAR Imaging. *Remote Sensing* 17, 1 (2024), 38. doi:10.3390/rs17010038

[51] Zhenghuan Xia, Zhilong Zhao, Tao Zhang, Dunge Liu, Huifeng Shi, Fuzhan Yue, and Tao Peng. 2021. A Novel Method of Space-borne Cognitive SAR Signal Generation Based on FPGA and DDS. In *IET IRC*, Vol. 2020. IET, 1600–1605. doi:10.1049/icp.2021.0520

[52] Yimin Zhao, Weibo Wang, Xiong Wang, Linghe Kong, Jiadi Yu, Yifei Zhu, Shiyuan Li, Chong He, and Guihai Chen. 2025. B2LoRa: Boosting LoRa Transmission for Satellite-IoT Systems with Blind Coherent Combining. In *ACM MobiCom*. Hong Kong, China. doi:10.1145/3680207.3723463

[53] Bowen Zheng and Fan Liu. 2024. Random Signal Design for Joint Communication and SAR Imaging Towards Low-Altitude Economy. *IEEE Wireless Communications Letters (WCL)* 13, 10 (2024), 2662–2666. doi:10.1109/LWC.2024.3432892

[54] Wenxing Zhou, Ruoyu Zhang, Guangyi Chen, and Wen Wu. 2022. Integrated Sensing and Communication Waveform Design: A Survey. *IEEE Open Journal of the Communications Society (OJ-COMS)* 3 (2022), 1930–1949. doi:10.1109/OJCOMS.2022.3215683

A Programmable Passive Metasurface

Appendices are supporting material that has not been peer-reviewed.

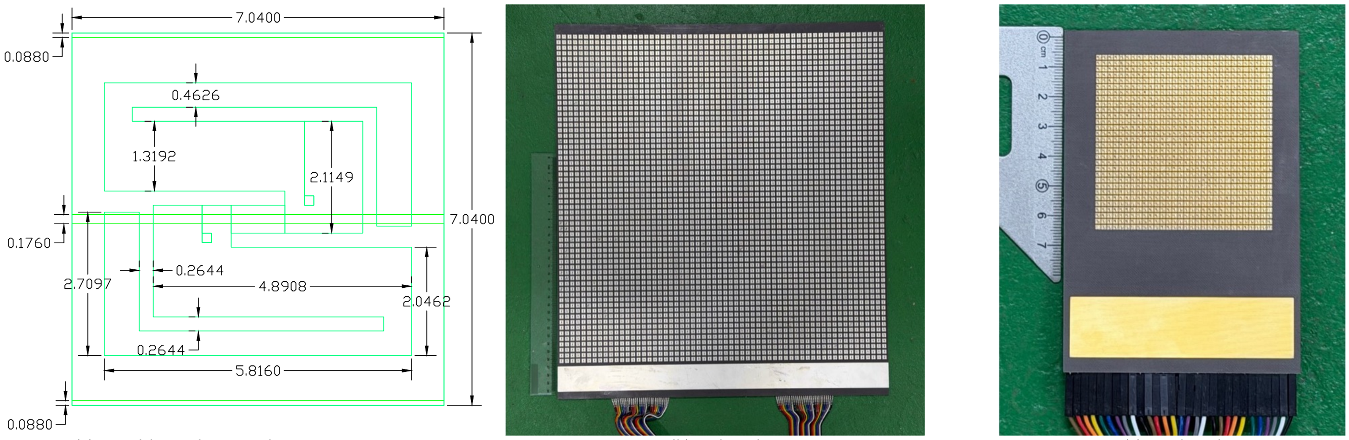

(a) Double-L element dimensions (b) X-band (c) Ka-band

Figure 16: Programmable passive metasurface details: (a) Double-L dimension ratios of the wideband phase modulation element; (b, c) fabricated physical prototypes of the *CommSAR* X-band and Ka-band metasurfaces (front view).

B Full-resolution SAR and *CommSAR* Imaging Results

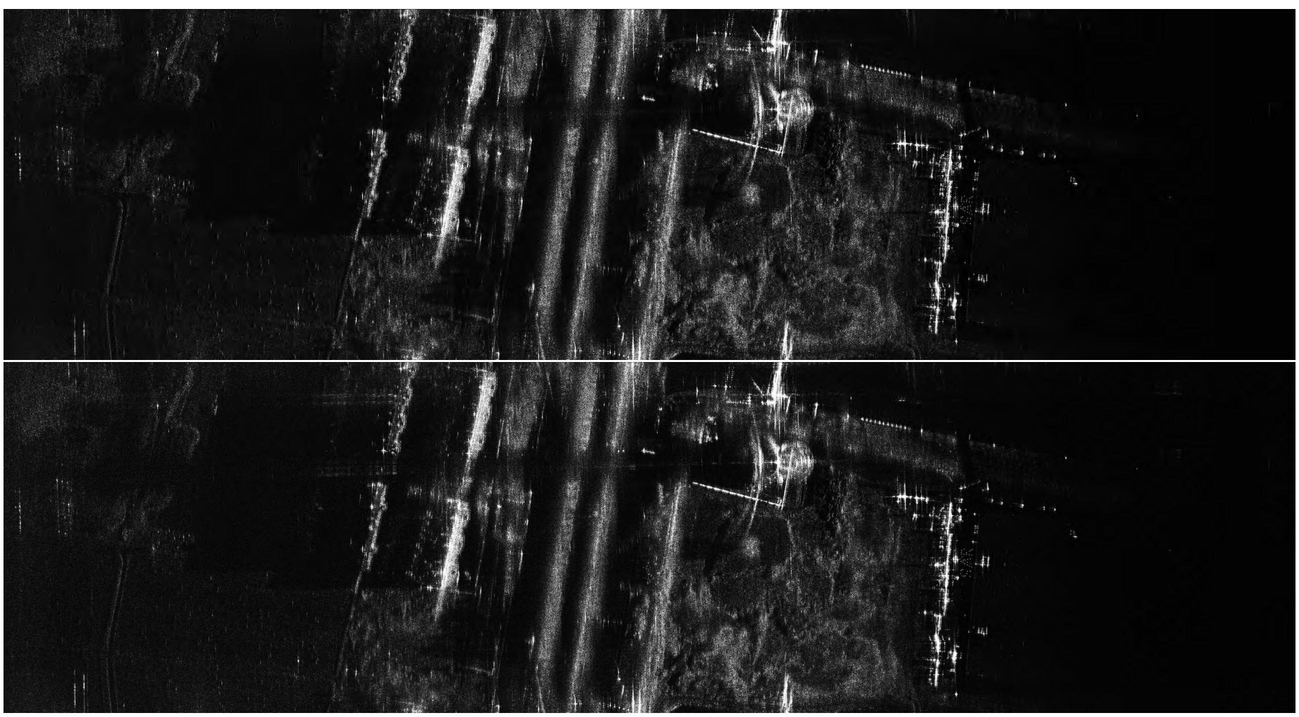

Figure 17: Full-resolution SAR (top) and *CommSAR* (bottom) imaging results for Flight #1 (256-symbol modulation).

Figure 18: Full-resolution SAR (top) and *CommSAR* (bottom) imaging results for Flight #2 (512-symbol modulation).

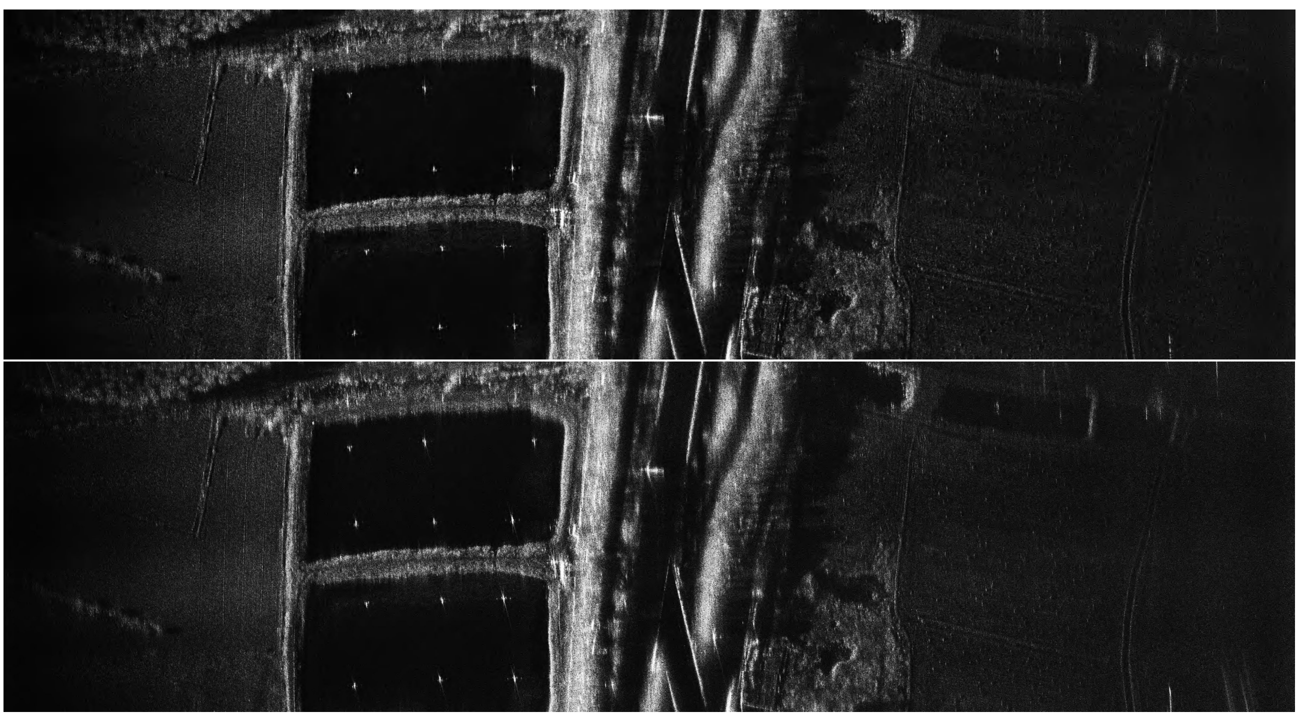

Figure 19: Full-resolution SAR (top) and *CommSAR* (bottom) imaging results for Flight #3 (1024-symbol modulation).